

# Numerical Scheme for the Generalised Serre-Green-Naghdi Model

Jordan Pitt<sup>a,\*</sup>, Christopher Zoppou<sup>a</sup>, Stephen Roberts<sup>a</sup>

<sup>a</sup>*Australian National University, Canberra*

---

## Abstract

A numerical scheme for solving the recently derived generalised Serre-Green-Naghdi equations which produce a family of equations modelling waves in shallow water with varying dispersion relationships, is described. The numerical scheme extends schemes applied to the classical Serre-Green-Naghdi equations written in conservation law form and is the first validated scheme for all admitted dispersion relationships. A typical second-order implementation of this numerical scheme is then demonstrated and validated using known analytic solutions; the travelling solitary wave and the dam-break problem. The numerical method is further validated for general members of the family of equations using forced solutions. Select members of this family are then used to simulate the evolution of rectangular waves of depression for which there are experimental results. The numerical method is shown to be conservative, robust and second-order accurate for the entire family of equations. The validated numerical solutions support a classification of the family of equations based on their linear dispersive properties which includes advancing dispersive wave trains in contrast to classical trailing dispersive wave trains.

---

## 1. Introduction

Water waves are well described by the elegant yet difficult to solve inviscid Euler equations. Owing to the difficulty of solving the Euler equations various approximate equations have been derived to model water waves in various regimes of the fundamental scales involved in the problem [1]. The shallow water regime, where the typical water depth  $h_0$  is much smaller than the wavelength  $\lambda$ , so that the shallowness parameter  $\sigma = h_0/\lambda \ll 1$  is one such regime which includes tsunamis, storm surges and bores [2]. The shallow water regime is characterised by nonlinearity where higher waves travel faster resulting in wave steepening. Recent advances in modelling waves in the shallow water regime have focused on the inclusion of dispersion [3], where waves of different frequencies travel at different speeds resulting in the breakdown of steep waves into so called dispersive wave trains [4]. The generalised Serre-Green-Naghdi Equations (gSGNE) recently derived by Clamond and Dutykh [5] are one such family of dispersive nonlinear equations that model waves in the shallow water regime. The gSGNE are a family of equations that generalise the classical nonlinear dispersive Serre-Green-Naghdi Equations (SGNE) first derived by Serre [6] with the addition of two free parameters  $\beta_1$  and  $\beta_2$ . These free parameters allow the gSGNE to exhibit linear dispersion relationships that well approximate the dispersion relationship of the linear wave theory [7] up to order  $\mathcal{O}(\sigma^6)$  terms [5, 8]. The gSGNE are thus of great interest to the wave modelling community.

Dispersive nonlinear shallow water wave equations, such as the gSGNE, are difficult to solve numerically due to the interaction between the nonlinear and dispersive effects with even seemingly trivial changes in initial conditions producing different behaviours in numerical solutions [9]. Typical numerical methods employed are finite element methods [8], discontinuous Galerkin methods [10, 11, 12], hybrid finite volume methods [13, 14] and splitting methods [15, 16, 17]. The gSGNE exacerbate these difficulties by allowing the relative strength of dispersion to vary with the choice of  $\beta_1$  and  $\beta_2$ , which even allows for non-dispersive equations termed the regularised shallow water wave equations [5]. A pseudo-spectral method [18] was employed to solve the regularised shallow water wave equations [5] and the improved SGNE which are accurate up to  $\mathcal{O}(\sigma^6)$  terms in the dispersion relationship [8]. However, the numerical method required anti-alias filtering to solve the regularised shallow water wave equations. This makes it unsuitable to seamlessly solve arbitrary members of

---

\*jpapitt@gmail.com

this family of nonlinear dispersive wave equations due to the sensitivity of high frequency structures in solutions [9] affected by anti-alias filtering.

In previous work we have developed and validated explicit numerical methods for a conservative reformulation of the SGNE [19, 14, 20, 21] given by  $\beta_1 = 2/3$  and  $\beta_2 = 0$  in the gSGNE. These numerical methods have all been based on the following approach: first solve an auxiliary elliptic equation for the non-conservative quantity and secondly evolve the equations in conservation law form using the finite volume method which requires the non-conserved quantity. The benefits of the approach was its ability to maintain the fundamental conservation properties of the SGNE [21], the robustness of the method in the presence of steep gradients, its ability to resolve high frequency structures [9] and lack of additional processing such as anti-alias filtering. The approach has been shown to produce the theoretical accuracy of the underlying methods [20, 21] with the desired conservation and linear dispersion properties [21]. It was demonstrated by Clamond and Dutykh [5] that the gSGNE can also be written in conservation law form and thus the technique described above for the SGNE can be extended to the gSGNE with arbitrary  $\beta_1$  and  $\beta_2$ .

This paper begins by introducing the gSGNE and highlighting their important properties. Of particular note, the free parameters  $\beta_1$  and  $\beta_2$  provide control of the width and relative location of the dispersive wave train. This allows for the family of equations to be classified by their respective dispersive wave train limits, and provides the basis for previously unobserved behaviour of dispersive wave trains. The second-order extension of the numerical scheme of Zoppou et al. [20] is then described. The numerical method is then validated against analytic solutions of the SGNE and the shallow water wave equations (SWWE) which are solutions of the gSGNE for the appropriate  $\beta$  values, demonstrating its convergence rate and conservation properties. Forced solutions are also used to validate that all terms in the gSGNE are being approximated to the correct order of accuracy with arbitrary  $\beta_1$  and  $\beta_2$  values. Forced solutions are necessary to validate the numerical method for other members of this family of equations, because no analytic solutions are currently known. Finally, various members of the gSGNE family are compared to experimental results for the evolution of rectangular depression waves to demonstrate the necessity of including dispersion and the effect of improving the accuracy of the dispersion relationship in realistic fluid problems. Together these validations demonstrate the capability of the numerical scheme to produce robust and accurate numerical solutions and the ability of the scheme to reproduce experimental results. Thus the first numerical scheme capable of solving the gSGNE for arbitrary values of  $\beta_1$  and  $\beta_2$  is produced and validated.

## 2. Generalised Serre-Green-Naghdi Equations

The gSGNE were derived by Clamond and Dutykh [5] using a Lagrangian field theory approach. These equations generalise the SGNE that describe a depth averaged approximation to the Euler equations, where  $h(x, t)$  is the water depth,  $u(x, t)$  is the depth averaged horizontal velocity and  $g$  is the acceleration due to gravity. This generalisation is achieved by introducing two free parameters  $\beta_1$  and  $\beta_2$ , each pair of  $\beta$  values corresponding to one member of this family of equations. In particular, the family of equations captured by gSGNE contains the SWWE, the SGNE, a family of regularised SWWE studied by Clamond and Dutykh [5] and a family of improved dispersion SGNE equations studied by Clamond et al. [8].

The gSGNE describe the conservation of mass ( $h$ ), momentum ( $uh$ ) and energy ( $\mathcal{E}$ ) for free surface water waves subject to gravitational forces like so

$$\frac{\partial h}{\partial t} + \frac{\partial(hu)}{\partial x} = 0 \quad (1a)$$

$$\frac{\partial(hu)}{\partial t} + \frac{\partial}{\partial x} \left( hu^2 + \frac{1}{2}gh^2 + \frac{1}{2}h^2\Gamma \right) = 0 \quad (1b)$$

$$\frac{\partial(\mathcal{E})}{\partial t} + \frac{\partial}{\partial x} \left[ hu \left( \frac{1}{2}u^2 + \frac{1}{4}\beta_1 h^2 \frac{\partial u}{\partial x} \frac{\partial u}{\partial x} + gh \left( 1 + \frac{1}{4}\beta_2 \frac{\partial h}{\partial x} \frac{\partial h}{\partial x} \right) + \frac{1}{3}h\Gamma \right) + \frac{1}{2}\beta_2 gh^3 \frac{\partial h}{\partial x} \frac{\partial u}{\partial x} \right] = 0 \quad (1c)$$

where

$$\Gamma = \beta_1 h \left[ \frac{\partial u}{\partial x} \frac{\partial u}{\partial x} - \frac{\partial^2 u}{\partial x \partial t} - u \frac{\partial^2 u}{\partial x^2} \right] - \beta_2 g \left[ h \frac{\partial^2 h}{\partial x^2} + \frac{1}{2} \frac{\partial h}{\partial x} \frac{\partial h}{\partial x} \right] \quad (1d)$$

$$\mathcal{E} = \frac{1}{2}hu^2 + \frac{1}{4}\beta_1 h^3 \frac{\partial u}{\partial x} \frac{\partial u}{\partial x} + \frac{1}{2}gh^2 \left( 1 + \frac{1}{2}\beta_2 \frac{\partial h}{\partial x} \frac{\partial h}{\partial x} \right). \quad (1e)$$

When  $\beta_1 = \beta_2 = 0$  these equations reduce to the SWWE and the SGNE are recovered when  $\beta_1 = 2/3$  and  $\beta_2 = 0$ .

Equation (1) contains three partial differential equations with only two unknowns,  $h$  and  $u$ . Since there are only two unknowns it is sufficient to solve only two of the three equations, typically either the conservation of mass (1a) and the conservation of momentum equations (1b) or the conservation of mass (1a) and the conservation of energy equations (1c). If  $h$  and  $u$  are sufficiently smooth, then the solution of any pair of these equations will produce identical results. However for non-smooth solutions of  $h$  and  $u$  these pairs of equations will produce different results [22]. Since the mass (1a) and momentum (1b) equations are commonly solved this results in dissipation of energy around discontinuities in the solution. Conversely, when the mass (1a) and energy equations (1c) are solved this results in dissipation of momentum and an incorrect propagation speed for discontinuities in the solution.

When solutions are sufficiently smooth all equations hold simultaneously and the total amounts of all these quantities remain constant in time if the system is closed. This can be seen by integrating (1) over the domain, and observing that the temporal derivative of the spatial integrals of mass ( $h$ ), momentum ( $uh$ ) and energy ( $\mathcal{E}$ ) is zero when there is no flux across the domain boundaries. This conservation property of the gSGNE will be used to validate the numerical method and its solution.

### 2.1. Linearised gSGNE

The linear dispersion properties of water wave equations have been of particular interest [8, 16, 23], as the scope of wave modelling expands to include dispersive effects. Indeed, the gSGNE are especially relevant because they provide better dispersion properties when compared to the linear theory for water waves [7] than the SWWE where  $\beta_1 = \beta_2 = 0$ .

The linearised gSGNE (1) are obtained by considering small perturbations,  $h_1(x, t)$  in depth and  $u_1(x, t)$  in velocity with a background mean water depth  $h_0$  and a mean velocity  $u_0$ . By using these assumptions and neglecting all terms significantly smaller than the perturbations we arrive at the linearised gSGNE

$$\frac{\partial h_1}{\partial t} + \frac{\partial}{\partial x} (u_0 h_1 + h_0 u_1) = 0 \quad (2a)$$

$$\frac{\partial u_1}{\partial t} + \frac{\partial}{\partial x} \left( u_0 u_1 + g h_1 - \frac{\beta_1}{2} h_0^2 \left[ \frac{\partial^2 u_1}{\partial x \partial t} + u_0 \frac{\partial^2 u_1}{\partial x^2} \right] - \frac{\beta_2}{2} g h_0^2 \frac{\partial^2 h_1}{\partial x^2} \right) = 0. \quad (2b)$$

The presence of the  $\beta_2$  term and the choice of  $\beta_1$  values distinguishes the linearised gSGNE from the linearised SGNE [20].

#### 2.1.1. Dispersion Relation

The dispersion relationship of the linearised gSGNE is obtained by seeking non-trivial travelling wave solutions of the form  $\exp(i(kx - \omega t))$  of (2) for  $h_1(x, t)$  and  $u_1(x, t)$ . By substituting in the assumed solution form, we obtain the following relationship between the frequency  $\omega$  in time and the wavenumber  $k$  in space

$$\omega_{\text{gSGNE}}^{\pm} = u_0 k \pm k \sqrt{g h_0} \sqrt{\frac{\beta_2 h_0^2 k^2 + 2}{\beta_1 h_0^2 k^2 + 2}}. \quad (3)$$

The dispersion relation has a positive and negative branch corresponding to the direction of these waves. This dispersion relation (3) is equivalent to the dispersion relation derived by Clamond and Dutykh [5] for the gSGNE who assumed that  $u_0 = 0$ .

The dispersion relationship for the linear water wave theory [7] is

$$u_0 k \pm \sqrt{g k \tanh(k h_0)}. \quad (4)$$

The power series approximations to the linear dispersion relationship of the gSGNE (3) and the linear water wave theory (4) are

$$\omega_{\text{gSGNE}}^{\pm} = \left( u_0 \pm \sqrt{g h_0} \right) k \pm \frac{(\beta_2 - \beta_1)}{4} \sqrt{g h_0} h_0^2 k^3 \pm \frac{(3\beta_1^2 - 2\beta_2\beta_1 - \beta_2^2)}{32} \sqrt{g h_0} h_0^4 k^5 + \mathcal{O}(k^7) \quad (5a)$$

$$\omega_{\text{linear}}^{\pm} = \left( u_0 \pm \sqrt{g h_0} \right) k \pm \frac{-1}{6} \sqrt{g h_0} h_0^2 k^3 \pm \frac{19}{360} \sqrt{g h_0} h_0^4 k^5 + \mathcal{O}(k^7). \quad (5b)$$

Comparing (5a) and (5b), allows the accuracy of the gSGNE dispersion relationship to be determined. In particular, the gSGNE are  $k^2$  accurate for all  $\beta$  values, accurate to the  $k^4$  term when  $\beta_1 = \beta_2 + 2/3$  and accurate up to the  $k^6$  term when  $\beta_1 = \beta_2 + 2/3$  and  $\beta_2 = 2/15$  [8].

From the dispersion relation (3), the phase speed  $v_p$  and the group speed  $v_g$  are

$$v_p^\pm = \frac{\omega_{\text{gSGNE}}^\pm}{k} = u_0 \pm \sqrt{gh_0} \sqrt{\frac{\beta_2 h_0^2 k^2 + 2}{\beta_1 h_0^2 k^2 + 2}}, \quad (6a)$$

$$v_g^\pm = \frac{\partial \omega_{\text{gSGNE}}^\pm}{\partial k} = u_0 \pm \sqrt{gh_0} \sqrt{\frac{\beta_2 h_0^2 k^2 + 2}{\beta_1 h_0^2 k^2 + 2}} \left[ 1 + \frac{\beta_2 - \beta_1}{(\frac{1}{2}\beta_2 h_0^2 k^2 + 1) ((\beta_1 - \frac{1}{3}) h_0^2 k^2 + 1)} \right]. \quad (6b)$$

### 2.1.2. Phase Speed Bounds

The numerical methods for the SGNE described by Le Métayer et al. [13] and Zoppou et al. [20] required that the phase speeds were bounded. To extend these methods to the gSGNE we must demonstrate that the phase speeds of the gSGNE are also bounded.

To demonstrate that the phase speeds are bounded, observe that when  $\beta_1 \geq 0$ ,  $\beta_2 \geq 0$  and  $h_0 k \geq 0$  then

$$f(h_0 k) = \frac{\beta_2 (h_0 k)^2 + 2}{\beta_1 (h_0 k)^2 + 2},$$

is a monotone function over  $h_0 k$ . This can be seen by reformulating and taking the derivative with respect to  $h_0 k$ , to obtain that

$$\frac{\partial (f(h_0 k))}{\partial (h_0 k)} = [\beta_2 - \beta_1] \frac{4 (h_0 k)}{(\beta_1 (h_0 k)^2 + 2)^2}.$$

The derivative is greater than zero and thus  $f(h_0 k)$  is monotone non-decreasing if  $\beta_1 \leq \beta_2$ . Whilst the derivative is greater than zero and thus  $f(h_0 k)$  is monotone non-increasing if  $\beta_1 \geq \beta_2$ . Since  $v_p^+ = u_0 + \sqrt{gh_0 f(h_0 k)}$  and  $v_p^- = u_0 - \sqrt{gh_0 f(h_0 k)}$ , given the above properties of  $f(h_0 k)$  under the initial assumptions  $v_p^+$  is monotone non-decreasing and  $v_p^-$  is monotone non-increasing when  $\beta_1 \leq \beta_2$ . Conversely, when  $\beta_1 \geq \beta_2$  then  $v_p^+$  is monotone non-increasing and  $v_p^-$  is monotone non-decreasing.

In addition to the monotonicity of  $v_p^\pm$ , when  $k \rightarrow 0$  then  $v_p^\pm \rightarrow u_0 \pm \sqrt{gh_0}$  and as  $k \rightarrow \infty$  then  $v_p^\pm \rightarrow u_0 \pm \sqrt{gh_0} \sqrt{\beta_2/\beta_1}$ . Therefore,  $v_p^\pm$  is monotonic and bounded at the limits of the domain, and thus bounded for all  $\beta$  values provided that  $\beta_1 = 0$  when  $\beta_2 = 0$ , otherwise in the  $k \rightarrow \infty$  limit the phase speed is no longer bounded. Consequently, the methods of Le Métayer et al. [13] and Zoppou et al. [20] for the SGNE can be extended to the gSGNE because the phase speeds are bounded.

In addition, to the phase speed bounds we also have the following chain of inequalities when  $\beta_1 \geq \beta_2$

$$u_0 - \sqrt{gh_0} \leq v_p^- \leq u_0 - \sqrt{gh_0} \sqrt{\frac{\beta_2}{\beta_1}} \leq u_0 \leq u_0 + \sqrt{gh_0} \sqrt{\frac{\beta_2}{\beta_1}} \leq v_p^+ \leq u_0 + \sqrt{gh_0}. \quad (7)$$

We designate this region of  $\beta$  values, as ‘Region 1’. In this region the minimum and maximum phase speed values are  $u_0 - \sqrt{gh_0}$  and  $u_0 + \sqrt{gh_0}$  respectively. Region 1 is then characterised by trailing dispersive waves when  $\beta_2 < \beta_1$  with an upper boundary where waves are not dispersive when  $\beta_2 = \beta_1$ . Region 1 includes the SWWE and the SGNE and is consistent with the behaviour of the dispersive waves given by the linear theory for water waves [7].

When  $\beta_2 > \beta_1$  the inequality chain becomes

$$u_0 - \sqrt{gh_0} \sqrt{\frac{\beta_2}{\beta_1}} \leq v_p^- \leq u_0 - \sqrt{gh_0} \leq u_0 \leq u_0 + \sqrt{gh_0} \leq v_p^+ \leq u_0 + \sqrt{gh_0} \sqrt{\frac{\beta_2}{\beta_1}} \quad (8)$$

This will be denoted as ‘Region 2’ and it is characterised by advancing dispersive waves. Since we are only interested in water waves with trailing dispersive waves, this paper will be restricted to studying waves in Region 1, although the numerical scheme is valid for all regions.

The regions and location of important members of the gSGNE in terms of  $\beta$  values is summarised in Figure 1. All equations in the gSGNE family are accurate up to  $\mathcal{O}(k^2)$  in the dispersion relationship (5). Furthermore, there is a family of equations that obtain  $\mathcal{O}(k^4)$  accuracy in the dispersion relationship. Only one particular member of this family, the improved SGNE, obtains a dispersion relationship which is  $\mathcal{O}(k^6)$  accurate. Additionally, there are illustrative numerical solutions that demonstrate the effect of the  $\beta$  values and hence the different dispersion relationships on solutions to the dam-break problem described in Section 4.2. The dam-break problem consists of initially still water with a left water depth of  $2m$  and a right water depth of  $1m$  with a discontinuous jump between the two. The numerical solutions have been well resolved using 25600 cells and the simulated water depth  $h$  at  $t = 35s$  is plotted. The same numerical solver has been used for each with the only change being the  $\beta$  parameters.

The numerical solutions for the SWWE compare well to the analytic solutions for the SWWE in Section 4.2, and the numerical solutions of the SGNE compare well to the study of the dam-break problems performed by Pitt et al. [9] for the SGNE. By comparing the numerical solution to its location in the  $\beta$  plot we can see that the behaviour of solutions is described well by the chain of inequalities (7) when  $\beta_1 \geq \beta_2$  and (8) when  $\beta_1 < \beta_2$ . In particular, for the SWWE and the regularised SWWE  $\beta_1 = \beta_2$  which results in a phase speed which is independent of  $k$  and thus there is no dispersion. Consequently, we observe no wave train between the shock and the rarefaction fan for these non-dispersive wave models. For the dispersive wave models such as the classical SGNE and the improved SGNE with  $\mathcal{O}(k^4)$  and  $\mathcal{O}(k^6)$  accuracy in the dispersion relationship respectively, we observe a dispersive wave train between the shock and the rarefaction fan. In Region 2 of the  $\beta$  plot we observe advancing dispersive wave trains behind the rarefaction fan and ahead of the shock due to the change of the chain of inequalities when  $\beta_1 < \beta_2$  in (8).

## 2.2. Alternative Conservative Form of the gSGNE

Clamond and Dutykh [5] provided a reformulation of (1b) for the gSGNE, analogous to the reformulation of the SGNE [20, 13, 24]. The purpose of this reformulation is to remove the mixed spatial-temporal derivative in the flux term of the momentum equation (1b), which is difficult to treat numerically. This reformulation is obtained by introducing a new conserved quantity

$$G = hu - \frac{\beta_1}{2} \frac{\partial}{\partial x} \left( h^3 \frac{\partial u}{\partial x} \right)$$

and thus (1b) can be written in conservation law form for  $G$  as

$$\frac{\partial G}{\partial t} + \frac{\partial}{\partial x} \left( uG + \frac{gh^2}{2} - \beta_1 h^3 \frac{\partial u}{\partial x} \frac{\partial u}{\partial x} - \frac{1}{2} \beta_2 gh^2 \left[ h \frac{\partial^2 h}{\partial x^2} + \frac{1}{2} \frac{\partial h}{\partial x} \frac{\partial h}{\partial x} \right] \right) = 0$$

When  $\beta_1 = 2/3$  then  $G$  is the same conserved quantity introduced for the SGNE [20, 13, 24].

This reformulation, provides the gSGNE in conservation law form for both  $h$  and the new conserved quantity  $G$ . Thus the conservative gSGNE are

$$\frac{\partial h}{\partial t} + \frac{\partial(uh)}{\partial x} = 0 \tag{9a}$$

$$\frac{\partial G}{\partial t} + \frac{\partial}{\partial x} \left( uG + \frac{gh^2}{2} - \beta_1 h^3 \frac{\partial u}{\partial x} \frac{\partial u}{\partial x} - \frac{1}{2} \beta_2 gh^2 \left[ h \frac{\partial^2 h}{\partial x^2} + \frac{1}{2} \frac{\partial h}{\partial x} \frac{\partial h}{\partial x} \right] \right) = 0. \tag{9b}$$

with

$$G = uh - \frac{\beta_1}{2} \frac{\partial}{\partial x} \left( h^3 \frac{\partial u}{\partial x} \right). \tag{9c}$$

Now that the gSGNE are written in conservation law form and have a bound on the phase speeds, they can be solved numerically using the hybrid finite volume technique described by Zoppou et al. [20] for the SGNE.

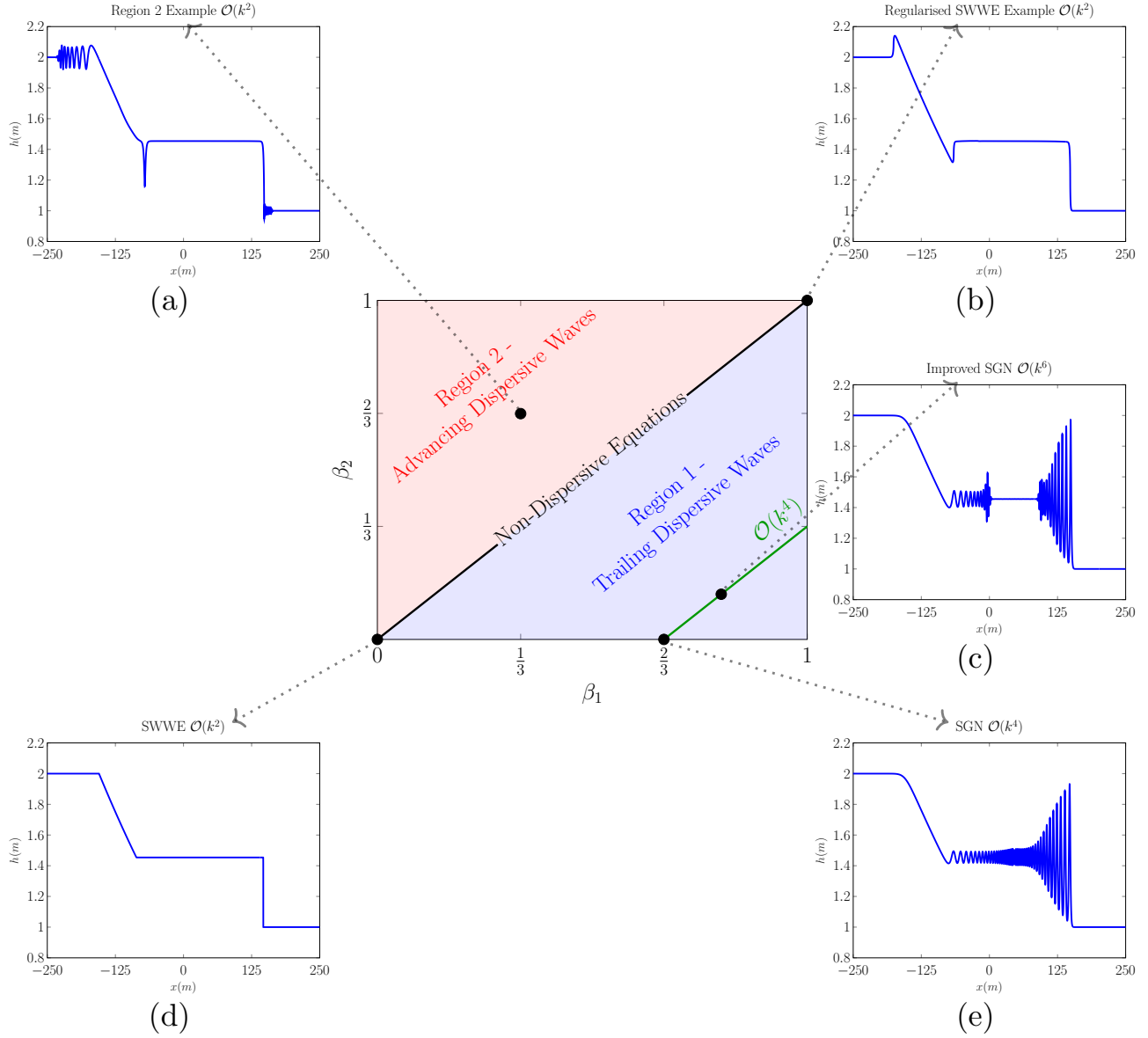


Figure 1: Phase speed regions of gSGNE in terms of  $(\beta_1, \beta_2)$  showing important equations, their associated dispersion relationship accuracy and an example numerical solution for the dam-break problem solved using  $\beta_1 = 1/3$  and  $\beta_2 = 2/3$  in (a),  $\beta_1 = \beta_2 = 1$  in (b),  $\beta_1 = 2/3 + 2/15$  and  $\beta_2 = 2/15$  in (c),  $\beta_1 = \beta_2 = 0$  in (d) and  $\beta_1 = 2/3$  and  $\beta_2 = 0$  in (e).

### 3. Numerical Scheme

The proposed numerical scheme for the gSGNE extends those previously published for the SGNE [20, 13] to allow any  $\beta$  values and the associated additional terms. We begin the description of the numerical scheme by giving a brief outline of the finite volume method and the discretisation therein. We then provide an overview of the numerical technique and then describe the simplest second-order implementation of this scheme in detail. With previous studies [20, 21] showing the sufficiency and necessity of second-order methods for the SGNE.

#### 3.1. Finite Volume Method and Discretisation

The core of these hybrid finite volume methods for the gSGNE is the finite volume method used to solve the equations in conservation law form. The finite volume method solves equations of the form

$$\frac{\partial q}{\partial t} + \frac{\partial f(q)}{\partial x} = 0 \quad (10)$$

where  $q$  is a generic conserved quantity. This is the form of the gSGNE after the reformulation (9). In the finite volume method (10) is integrated over cells of fixed width  $\Delta x$  in space and over time steps of fixed length  $\Delta t$ . The midpoint of the  $j^{th}$  cell is given by  $x_j = x_0 + j\Delta x$  while the cell edges of the  $j^{th}$  cell are given by  $x_{j-1/2} = x_0 + (j - \frac{1}{2})\Delta x$  and  $x_{j+1/2} = x_0 + (j + \frac{1}{2})\Delta x$ . Likewise the  $n^{th}$  time step is given by  $t^n = t^0 + n\Delta t$ .

Integrating (10) over both space and time results in

$$\bar{q}_j^{n+1} = \bar{q}_j^n + \frac{\Delta t}{\Delta x} [F_{j+1/2}^n - F_{j-1/2}^n] \quad (11)$$

where

$$\bar{q}_j^n = \frac{1}{\Delta x} \int_{x_{j-1/2}}^{x_{j+1/2}} q(x, t^n) dx$$

is the average of  $q$  over the  $j^{th}$  cell at time  $t^n$  and

$$F_{j\pm 1/2}^n = \frac{1}{\Delta t} \int_{t^n}^{t^{n+1}} f(q(x_{j\pm 1/2}, t)) dt$$

is the average flux of  $q$  across the cell edge from time  $t^n$  to  $t^{n+1}$ . Therefore, if  $F_{j\pm 1/2}^n$  can be approximated with the appropriate order of accuracy, then we have an explicit method for updating the cell average of the conserved quantities through time for equations in conservation law form (10).

#### 3.2. Overview

We will now describe the numerical scheme, which uses the above finite volume formulation to solve (9a) and (9b). When describing this broad overview it is also useful to consider collections of the point-wise values  $q$  or cell averaged values  $\bar{q}$  described above over the whole domain at a particular time. Thus for  $q$ , we define  $\mathbf{q}^n$  to be the vector of  $q_j^n$  values and  $\bar{\mathbf{q}}^n$  to be the vector of  $\bar{q}_j^n$  values for all cells in the domain at time  $t^n$ .

The numerical scheme for the gSGNE based on the finite volume method (11) then proceeds as follows. Begin at the  $n^{th}$  time step where the vectors of cell averages of the conserved quantities  $\bar{\mathbf{h}}^n$  and  $\bar{\mathbf{G}}^n$  are either known or provided as initial conditions.

1. Solve (9c) using  $\bar{\mathbf{h}}^n$  and  $\bar{\mathbf{G}}^n$  to obtain an approximation to  $\bar{\mathbf{u}}^n$ , which can be expressed as

$$\mathcal{A}(\bar{\mathbf{h}}^n, \bar{\mathbf{G}}^n) \rightarrow \bar{\mathbf{u}}^n.$$

2. Solve (9a) and (9b), using the finite volume method (11) with an approximate Riemann solver such as the one described by Kurganov et al. [25], to obtain  $\bar{h}_j^{n+1}$  and  $\bar{G}_j^{n+1}$  at the next time step, like so

$$\mathcal{F}(\bar{\mathbf{h}}^n, \bar{\mathbf{G}}^n, \bar{\mathbf{u}}^n) \rightarrow \bar{\mathbf{h}}^{n+1}, \bar{\mathbf{G}}^{n+1}.$$

3. Steps 1 and 2 are repeated and combined using a convex combination to obtain a Strong Stability Preserving (SSP) Runge Kutta time stepping method [26] to approximate  $\bar{\mathbf{h}}^{n+1}$  and  $\bar{\mathbf{G}}^{n+1}$  with the correct accuracy in time.

This numerical scheme produces the numerical methods of Le Métayer et al. [13], Zoppou et al. [20] and Pitt [21] when  $\beta_1 = 2/3$  and  $\beta_2 = 0$ . Additionally, when  $\beta_1 = \beta_2 = 0$  the gSGNE reduces to the SWWE, and this numerical scheme reduces to a traditional finite volume method [27].

### 3.3. Typical Second-Order Implementation

The description of this numerical method will be broken up into the steps described in Section 3.2 for simplicity and also to highlight the interchangeability of the different parts of the scheme.

#### 3.3.1. Step 1 - Solution of the Elliptic Equation

To solve (9c) given  $\bar{\mathbf{h}}^n$  and  $\bar{\mathbf{G}}^n$  to obtain  $\bar{\mathbf{u}}^n$  we use the observation that the cell average and the cell nodal value are equal up to second-order accuracy, so that  $\bar{\mathbf{q}}^n = \mathbf{q}^n + \mathcal{O}(\Delta x^2)$  for all the quantities of interest. Assuming that  $u$  is sufficiently smooth, then a second-order central finite difference approximation can be used to accurately solve (9c).

The second-order central finite difference approximation to (9c) can be written as

$$\mathbf{u}^n = \mathbf{A}^{-1} \mathbf{G}^n \quad (12)$$

where  $\mathbf{A}$  is a tri-diagonal matrix with the sub-diagonal, diagonal and super-diagonal elements given by

$$A_{j,j-1} = -\frac{\beta_1}{2} \left[ \frac{(h_j^n)^3}{\Delta x^2} - \frac{3(h_j^n)^2}{2\Delta x} \frac{h_{j+1}^n - h_{j-1}^n}{2\Delta x} \right] \quad (13a)$$

$$A_{j,j} = h_j^n + \beta_1 \frac{(h_j^n)^3}{\Delta x^2} \quad (13b)$$

$$A_{j,j+1} = -\frac{\beta_1}{2} \left[ \frac{(h_j^n)^3}{\Delta x^2} + \frac{3(h_j^n)^2}{2\Delta x} \frac{h_{j+1}^n - h_{j-1}^n}{2\Delta x} \right] \quad (13c)$$

respectively.

The finite difference approximation (12) can be solved with any matrix solver. We use the explicit Thomas Algorithm [28]. This is an efficient method provided  $\mathbf{A}$  is diagonally dominant which is the case as long as  $h_j^n > 0$ , which is true for all the problems of interest in this paper.

Thus as desired we have

$$\mathbf{A}(\bar{\mathbf{h}}^n, \bar{\mathbf{G}}^n) = \mathbf{A}^{-1} \mathbf{G}^n = \mathbf{u}^n \rightarrow \bar{\mathbf{u}}^n. \quad (14)$$

#### 3.3.2. Step 2 - Finite Volume Method - Reconstruction

The finite volume method of Kurganov et al. [25] relies on approximations of all the terms in the spatial derivative of the flux at the cell edges  $x_{j\pm 1/2}$ . Thus the following quantities require second-order approximations at the cell edges:  $u$ ,  $h$ ,  $G$ ,  $\partial u/\partial x$ ,  $\partial h/\partial x$ ,  $\partial^2 h/\partial x^2$ . In this paper we are interested in validating the numerical method by reproducing solutions to smooth analytic and forced solutions for all members of the gSGNE. We are also interested in validating the numerical method for the discontinuous dam-break solution for only the SWWE where  $\beta_1 = \beta_2 = 0$  and thus only  $h$ ,  $u$  and  $G = uh$  need to be approximated. For this reason our gSGNE solver uses approximations to  $u$ ,  $h$ ,  $G$  that allow for discontinuities and thus require limiting. Whereas the approximations to the derivatives  $\partial u/\partial x$ ,  $\partial h/\partial x$ ,  $\partial^2 h/\partial x^2$  will assume that these quantities are smooth and thus do not require limiting.

Figure 1 demonstrates the adequacy of this reconstruction approach even in situations where the derivatives are present in the equations but are not smooth. A main reason for this is that the elliptic equation (9c) helps control the smoothness of  $u$ . However, this does not explain why we get reasonable results when assuming the derivatives of  $h$  are smooth when they are not smooth in the initial conditions. For the validations performed in this paper, the assumption on the smoothness of the derivatives  $\partial u/\partial x$ ,  $\partial h/\partial x$ ,  $\partial^2 h/\partial x^2$  is adequate.

The reconstructions for  $u$ ,  $h$  and  $G$  will be summarised for a general quantity  $q$ . For the  $j^{th}$  cell we have the reconstruction at the left boundary  $q_{j-1/2}^+ = \bar{q}_j - s_j \Delta x/2$  and the reconstruction at the right boundary  $q_{j+1/2}^- = \bar{q}_j + s_j \Delta x/2$ . The slope of the reconstruction  $s_j$  is calculated like so

$$s_j = \text{minmod} \left( \theta \frac{\bar{q}_j - \bar{q}_{j-1}}{\Delta x}, \frac{\bar{q}_{j+1} - \bar{q}_{j-1}}{2\Delta x}, \theta \frac{\bar{q}_{j+1} - \bar{q}_j}{\Delta x} \right). \quad (15)$$

The minmod function is defined as follows

$$\text{minmod}(a, b, c) = \begin{cases} \min(a, b, c) & \text{when } a > 0, b > 0, c > 0 \\ \max(a, b, c) & \text{when } a < 0, b < 0, c < 0 \\ 0 & \text{otherwise} \end{cases}. \quad (16)$$



This gives a reconstruction at each cell edge, so cell  $j$  gives rise to  $q_{j-1/2}^+$  and  $q_{j+1/2}^-$  while cell  $j+1$  gives rise to  $q_{j+1/2}^+$  and  $q_{j+3/2}^-$ , all of which are required in the flux approximation.

For  $\partial u/\partial x$ ,  $\partial h/\partial x$  and  $\partial^2 h/\partial x^2$  we assume that the quantities are smooth, and so using the appropriate order finite difference approximation at the cell edges is sufficient. We demonstrate these approximations for  $x_{j+1/2}$  and a generic quantity  $q$

$$\begin{aligned}\left[\frac{\partial q}{\partial x}\right]_{j+1/2} &= \frac{q_{j+1} - q_j}{\Delta x}, \\ \left[\frac{\partial^2 q}{\partial x^2}\right]_{j+1/2} &= \frac{q_{j+2} - q_{j+1} - q_j + q_{j-1}}{2\Delta x^2}.\end{aligned}$$

### 3.3.3. Step 2 - Finite Volume Method - Flux Approximation

To solve (9a) and (9b) which are both in conservation law form (10) we use (11). Since we begin with  $\bar{\mathbf{h}}^n$  and  $\bar{\mathbf{G}}^n$ , we only require an approximation to  $F_{j\pm 1/2}^n$  to obtain  $\bar{\mathbf{h}}^{n+1}$  and  $\bar{\mathbf{G}}^{n+1}$ .

In this numerical scheme the approximate Riemann solver described by Kurganov et al. [25] is used to calculate  $F_{j\pm 1/2}^n$ . The major advantage of this scheme is that it only requires bounds on the phase speeds. Only the calculation of the flux term  $F_{j+1/2}^n$  is demonstrated as the process to calculate the flux term  $F_{j-1/2}^n$  is identical but with different cells. For  $q$  the flux is approximated by

$$F_{j+1/2}^n = \frac{a_{j+\frac{1}{2}}^+ f(q_{j+\frac{1}{2}}^-) - a_{j+\frac{1}{2}}^- f(q_{j+\frac{1}{2}}^+)}{a_{j+\frac{1}{2}}^+ - a_{j+\frac{1}{2}}^-} + \frac{a_{j+\frac{1}{2}}^+ a_{j+\frac{1}{2}}^-}{a_{j+\frac{1}{2}}^+ - a_{j+\frac{1}{2}}^-} [q_{j+\frac{1}{2}}^+ - q_{j+\frac{1}{2}}^-] \quad (17)$$

where  $a_{j+\frac{1}{2}}^+$  and  $a_{j+\frac{1}{2}}^-$  are given by the phase speed bounds and all quantities on the right hand side are computed at time  $t^n$ . Applying the phase speed bounds (7) and (8) we obtain

$$a_{j+\frac{1}{2}}^- = \min \left\{ 0, u_{j+1/2}^- - \max \left( 1, \sqrt{\frac{\beta_2}{\beta_1}} \right) \sqrt{gh_{j+1/2}^-}, u_{j+1/2}^+ - \max \left( 1, \sqrt{\frac{\beta_2}{\beta_1}} \right) \sqrt{gh_{j+1/2}^+} \right\}, \quad (18)$$

$$a_{j+\frac{1}{2}}^+ = \max \left\{ 0, u_{j+1/2}^- + \max \left( 1, \sqrt{\frac{\beta_2}{\beta_1}} \right) \sqrt{gh_{j+1/2}^-}, u_{j+1/2}^+ + \max \left( 1, \sqrt{\frac{\beta_2}{\beta_1}} \right) \sqrt{gh_{j+1/2}^+} \right\} \quad (19)$$

where the  $\max \left( 1, \sqrt{\beta_2/\beta_1} \right)$  accounts for the different phase speed bounds (7) and (8), which depend on the choice of  $\beta$  values.

The flux functions  $f(q_{j+\frac{1}{2}}^-)$  and  $f(q_{j+\frac{1}{2}}^+)$  are evaluated using the reconstructed values of the  $j^{th}$  and  $(j+1)^{th}$  cell respectively. From the continuity equation (9a) we have

$$f(h_{j+\frac{1}{2}}^\pm) = u_{j+1/2}^\pm h_{j+1/2}^\pm.$$

For the evolution of  $G$  equation (9b) we have

$$\begin{aligned}f(G_{j+\frac{1}{2}}^\pm) &= u_{j+1/2}^\pm G_{j+1/2}^\pm + \frac{g}{2} (h_{j+1/2}^\pm)^2 - \beta_1 (h_{j+1/2}^\pm)^3 \left( \left[ \frac{\partial u}{\partial x} \right]_{j+1/2} \right)^2 \\ &\quad - \frac{1}{2} \beta_2 g (h_{j+1/2}^\pm)^2 \left[ h_{j+1/2}^\pm \left[ \frac{\partial^2 h}{\partial x^2} \right]_{j+1/2} + \frac{1}{2} \left( \left[ \frac{\partial h}{\partial x} \right]_{j+1/2} \right)^2 \right] \quad (20)\end{aligned}$$

where the derivatives are assumed to be smooth across the cell edge, and thus do not require different superscripts.

Since the reconstructions were given above for all these quantities, we can approximate  $F_{j\pm 1/2}^n$  using (17) and thus employ (11) to obtain  $\bar{\mathbf{h}}^{n+1}$  and  $\bar{\mathbf{G}}^{n+1}$  resulting in

$$\mathcal{F}(\bar{\mathbf{h}}^n, \bar{\mathbf{G}}^n, \bar{\mathbf{u}}^n) = \bar{q}_j^n + \frac{\Delta t}{\Delta x} [F_{j+1/2}^n - F_{j-1/2}^n] \rightarrow \bar{\mathbf{h}}^{n+1}, \bar{\mathbf{G}}^{n+1} \quad (21)$$

as desired.

### 3.3.4. Step 3 - Runge-Kutta Time Stepping

Combining Steps 1 and Steps 2, provides a spatially second-order scheme with first-order time stepping. To arrive at a fully second-order method, we repeat Steps 1 and Steps 2 according to the second-order SSP Runge Kutta method [26]. Doing this we obtain the following scheme making use of the above implementation of  $\mathcal{A}$ , (14) and  $\mathcal{F}$ , (21)

$$\begin{aligned} \bar{\mathbf{h}}^{(1)}, \bar{\mathbf{G}}^{(1)} &= \mathcal{F}(\bar{\mathbf{h}}^n, \bar{\mathbf{G}}^n, \mathcal{A}(\bar{\mathbf{h}}^n, \bar{\mathbf{G}}^n)) \\ \bar{\mathbf{h}}^{(2)}, \bar{\mathbf{G}}^{(2)} &= \mathcal{F}(\bar{\mathbf{h}}^{(1)}, \bar{\mathbf{G}}^{(1)}, \mathcal{A}(\bar{\mathbf{h}}^{(1)}, \bar{\mathbf{G}}^{(1)})) \\ \bar{\mathbf{h}}^{n+1}, \bar{\mathbf{G}}^{n+1} &= \frac{1}{2}(\bar{\mathbf{h}}^n + \bar{\mathbf{h}}^{(2)}), \frac{1}{2}(\bar{\mathbf{G}}^n + \bar{\mathbf{G}}^{(2)}). \end{aligned}$$

obtaining a conditionally stable fully second-order method for solving (9).

### 3.4. Boundary Conditions

For the purposes of the validation below and for simplicity, we have applied Dirichlet boundary conditions using ghost cells over which the values of  $h$ ,  $G$  and  $u$  are known. Thus in addition to the  $m$  cells inside the boundary we have an additional  $l$  cells either side of it so that we have the left ghost cells  $-l, -l+1, \dots, -1$  and the right ghost cells  $m, m+1, \dots, m+l-1$ . Since the numerical method has a maximum stencil that extends 2 cells beyond the target cell, then  $l$  must be greater than 1.

This boundary condition is applied to Step 1 by extending the matrix equation (12) to vectors containing the ghost cells  $\hat{\mathbf{u}}^n$  and  $\hat{\mathbf{G}}^n$  like so

$$\begin{aligned} \hat{\mathbf{u}}^n &= [u_{-l}^n \dots u_{-1}^n u_0^n \dots u_{m-1}^n u_m^n \dots u_{m+l-1}^n]^T \\ \hat{\mathbf{G}}^n &= [G_{-l}^n \dots G_{-1}^n G_0^n \dots G_{m-1}^n G_m^n \dots G_{m+l-1}^n]^T. \end{aligned}$$

Likewise the associated extended matrix  $\hat{\mathbf{A}}$  in (12) is the same as  $\mathbf{A}$  when  $0 \leq j \leq m-1$  (13) with the additional ghost cell values given by

$$\hat{A}_{j,j-1} = 0 \quad \hat{A}_{j,j} = 1 \quad \hat{A}_{j,j+1} = 0$$

when  $j < 0$  or  $j > m-1$ .

For Step 2 there is no need to reconstruct the quantities inside the ghost cells because  $h$ ,  $G$  and  $u$  are given.

### 3.5. Courant-Frederichs-Lewy Condition

To ensure the stability of the finite volume method (11) the Courant-Friedrichs-Lewy (CFL) condition [29] is used. The CFL condition is necessary for stability and ensures that time steps are small enough so that information is only transferred between neighbouring cells. For the gSGNE the CFL condition is

$$\Delta t \leq \frac{Cr}{\max_j \{a_{j+1/2}^\pm\}} \Delta x \quad (22)$$

where  $a_{j+1/2}^\pm$  are the phase speed bounds used in the flux approximation (19) and  $0 \leq Cr \leq 1$  is the Courant number.

## 4. Validation

The numerical method described above is validated using analytic solutions for particular  $\beta$  values that correspond to the SGNE and the SWWE as well as a forced solution. Together these tests demonstrate the ability of the method to reproduce analytic solutions to important members of the gSGNE family, as well as assessing the accuracy of the numerical method's approximation of all terms in the gSGNE.

### 4.1. Convergence and Conservation Measures

To validate the numerical solutions we make use of measures of convergence and conservation. The measure of convergence will be the relative deviation of the numerical solution from the equivalent analytic or forced solution using the  $L_2$  norm. While the conservation properties of the numerical method will be measured by numerically approximating the energy in the initial conditions and the numerical solution and comparing them using a measure called  $C_1$ .

For a quantity  $q$  with a vector of its analytic or forced solution at the cell midpoints  $\mathbf{q}$  and the numerical solution at the cell midpoints  $\mathbf{q}^*$ , the discrete non-dimensional  $L_2$  norm is

$$L_2(\mathbf{q}, \mathbf{q}^*) = \left( \frac{\sum_j (q_j - q_j^*)^2}{\sum_j q_j^2} \right)^{\frac{1}{2}} \quad (23)$$

where the time-step superscripts were suppressed for simplicity.

For a quantity  $q$  with a vector of its values at the  $n^{th}$  time step  $\mathbf{q}^n$ , the total amount of the quantity is approximated by  $C(\mathbf{q}^n)$ . The method for this is the same as the method described by Zoppou et al. [20], which has a higher order of accuracy than the numerical method used to solve the gSGNE. Using the numerical approximation to the total amounts, the conservation error is obtained using

$$C_1(\mathbf{q}^0, \mathbf{q}^n) = \begin{cases} \frac{|C(\mathbf{q}^0) - C(\mathbf{q}^n)|}{|C(\mathbf{q}^0)|} & , \quad |C(\mathbf{q}^0)| > 0 \\ |C(\mathbf{q}^0) - C(\mathbf{q}^n)| & , \quad |C(\mathbf{q}^0)| = 0 \end{cases} \quad (24)$$

### 4.2. Analytic Solutions

The analytic solutions used to validate the numerical method, are the solitary travelling wave solution of the SGNE and the dam-break solution of the SWWE. The solitary travelling wave solution is a smooth travelling wave solution, where the nonlinear and dispersive terms are in balance in the gSGNE. Whereas the dam-break solution of the SWWE demonstrates the robustness of the method in the presence of steep gradients.

#### 4.2.1. SGNE - Solitary Travelling Wave Solution

When  $\beta_1 = 2/3$  and  $\beta_2 = 0$  the gSGNE are equivalent to the SGNE which admit the following travelling wave solution [4]

$$h(x, t) = a_0 + a_1 \text{sech}^2(\kappa(x - ct)), \quad (25a)$$

$$u(x, t) = c \left( 1 - \frac{a_0}{h(x, t)} \right), \quad (25b)$$

where

$$\kappa = \frac{\sqrt{3a_1}}{2a_0\sqrt{a_0 + a_1}} \quad (25c)$$

and

$$c = \sqrt{g(a_0 + a_1)} \quad (25d)$$

is the speed of the wave.

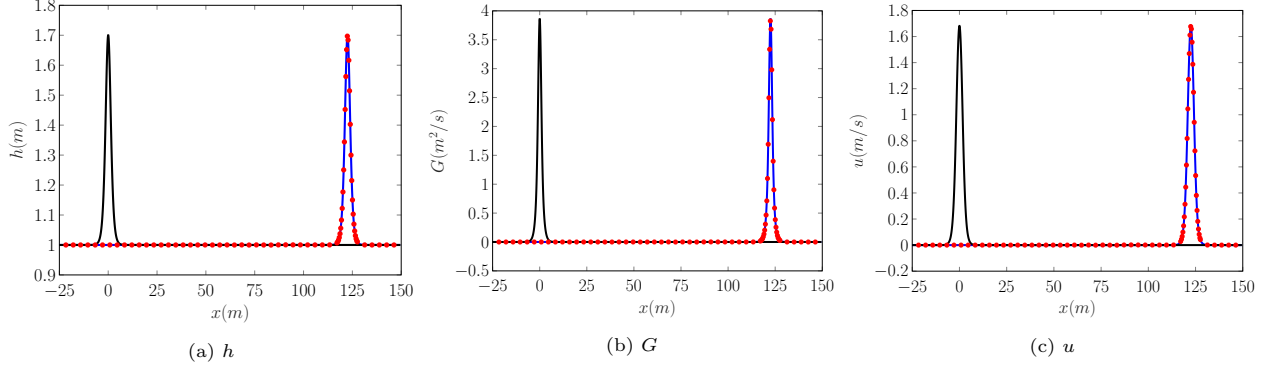


Figure 2: Plot of comparing initial (—), analytic solution (—), and numerical solution with  $\Delta x \approx 0.06m$  (•) to the solitary travelling wave analytic solution of the gSGNE when  $\beta_1 = 2/3$  and  $\beta_2 = 0$  at  $t = 30s$ .

This travelling wave solution is maintained due to a balance between the dispersive terms and the nonlinear terms in the momentum equation (1b). This balance results in a solitary wave that is advected with a constant speed without a changing shape. Validating the numerical solutions for the gSGNE solver using this solution tests the balance between these terms in (1b), and allows us to verify the method's conservation of energy as the solution is smooth. To enable a comparison between the numerical method and the SGNE solver of Zoppou et al. [20] and Pitt [21], the chosen solitary travelling wave parameters were  $a_0 = 1m$  and  $a_1 = 0.7m$  and the acceleration due to gravity at the Earth's surface,  $g = 9.81m^2/s$  was used.

The numerical solution was solved over the domain  $[-200m, 200m]$  from  $t = 0s$  until  $t = 30s$ . The spatial resolution was varied like so  $\Delta x = 400/(100 \times 2^l)$ , where  $l$  was increased from 0 to 12. To satisfy the CFL condition (22) the time step  $\Delta t = \Delta x / (2\sqrt{g(a_0 + a_1)})$  was chosen. The limiting parameter  $\theta = 1.2$ , was chosen to match previous numerical experiments [20, 21].

Example numerical solutions for  $h$ ,  $u$  and  $G$  with  $\Delta x = 400/(100 \times 2^6) \approx 0.06m$  are plotted in Figure 2. These examples demonstrate that the numerical solutions can reproduce the analytic solutions well.

The convergence properties of the method as  $\Delta x$  varies are given in Figure 3 where Figure 3a shows the  $L_2$  norm calculated over the whole domain and Figure 3b shows the  $L_2$  norm at the peak only. The  $L_2$  norm over the whole domain demonstrates that all quantities are approximated with second-order accuracy, and thus the method is second-order accurate. The  $L_2$  norm at the peak was measured by taking the relative difference between the numerical solutions value at the peak of the wave which are given by  $\max(\mathbf{h}^n)$ ,  $\max(\mathbf{u}^n)$  to the analytic values which are  $a_0 + a_1$  and  $a_0 c / (a_0 + a_1)$  respectively. The  $L_2$  norm at the peak demonstrates that even with the slope limiting and the diffusion introduced by the flux approximation [9], the numerical method introduces little diffusion and is second-order accurate.

The conservation error  $C_1$  (24) of the numerical solutions as  $\Delta x$  varies is given in Figure 4. This conservation measure demonstrates that the finite volume method conserves  $h$  and  $G$  up to round-off error, which accumulates as  $\Delta x$  increases due to the additional number of calculations. Since  $uh$  and  $\mathcal{E}$  are not conserved quantities in our finite volume method which solves (9a) and (9b), they are not conserved up to round-off error. However, the conservation properties of  $uh$  and  $\mathcal{E}$  are good, with both exhibiting conservation errors that have better than second-order convergence in  $\Delta x$ .

By locating the cell on which  $\mathbf{h}^n$  achieves its maximum, we can provide an upper and lower bound for the speed of the numerical solution to the travelling wave problem where the lower bound is  $c_-^* = (x_{\text{peak cell}} - 0.5\Delta x)/t$  and the upper bound is  $c_+^* = (x_{\text{peak cell}} + 0.5\Delta x)/t$ . These upper and lower bounds are compared to the analytic value  $c$  given by (25d) in Figure 5. This figure demonstrates the diffusion of the numerical scheme when  $\Delta x$  is large because both the upper and lower bounds on the wave speed are below the analytic value. However, this diffusion becomes negligible when  $\Delta x$  is small, and for the lowest  $\Delta x$  value we observe that  $c_-^* < c < c_+^*$ , indicating that the peak is travelling at the correct speed up to cell width accuracy.

These results agree well with the numerical solutions of Pitt [21], who compared various numerical methods for the SGNE. This demonstrates that the numerical method solving the gSGNE when  $\beta_1 = 2/3$  and  $\beta_2 = 0$  accurately reproduces the analytic solution of the SGNE.

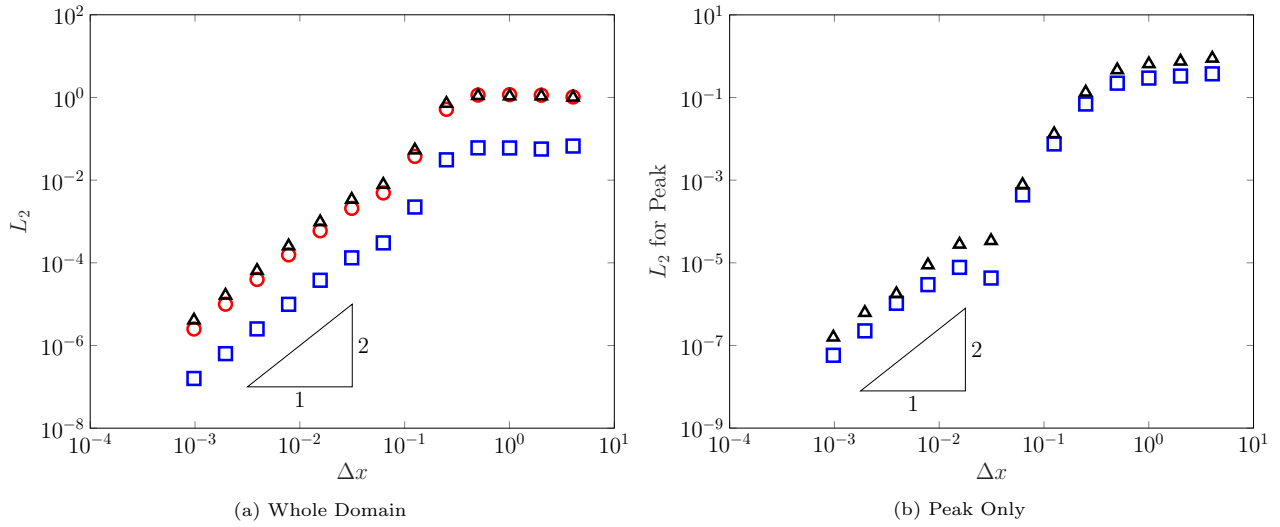


Figure 3: Convergence plots for  $h$  ( $\square$ ),  $G$  ( $\circ$ ) and  $u$  ( $\Delta$ ) for the numerical solutions of the gSGNE when  $\beta_1 = 2/3$  and  $\beta_2 = 0$  as  $\Delta x$  varies.

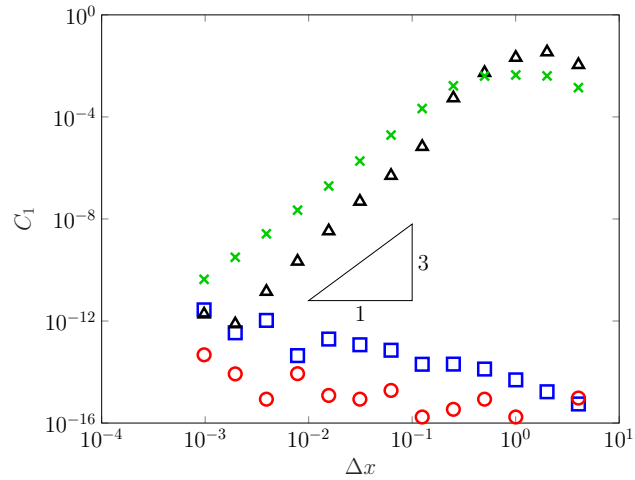


Figure 4: Conservation plot for  $h$  ( $\square$ ),  $G$  ( $\circ$ ),  $uh$  ( $\Delta$ ) and  $\mathcal{E}$  ( $\times$ ) for the numerical solutions of the gSGNE when  $\beta_1 = 2/3$  and  $\beta_2 = 0$  as  $\Delta x$  varies.

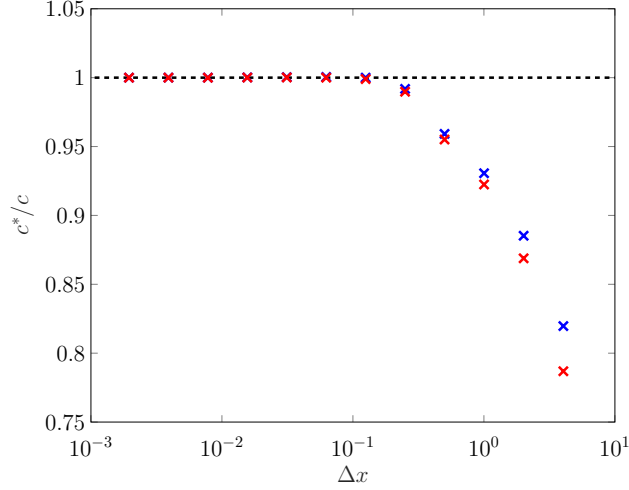


Figure 5: Plot of  $c_+^*/c$  (X),  $c_-^*/c$  (X) and the analytic value (— —) as  $\Delta x$  varies.

#### 4.2.2. SWWE - Dam-break Solution

When  $\beta_1 = \beta_2 = 0$  the gSGNE equations reduce to the SWWE. Consequently, (9b) and (1b) become identical with  $G = uh$ . The SWWE possess an analytic solution to the dam-break problem given by the initial conditions

$$h(x, 0) = \begin{cases} h_0 & x < 0 \\ h_1 & x \geq 0 \end{cases} \quad (26a)$$

$$u(x, 0) = 0 \quad (26b)$$

$$G(x, 0) = 0. \quad (26c)$$

The solution to the dam-break problem using the conservation of mass (1a) and momentum (1b) equations is given by

$$h(x, t) = \begin{cases} h_0 & , & x \leq -t\sqrt{gh_0} \\ \frac{4}{9g} \left( \sqrt{gh_0} - \frac{x}{2t} \right)^2 & , & -t\sqrt{gh_0} < x \leq t(u_2 - \sqrt{gh_2}) \\ h_2 & , & t(u_2 - \sqrt{gh_2}) < x \leq tS \\ h_1 & , & tS \leq x \end{cases} \quad (27a)$$

$$u(x, t) = \begin{cases} 0 & , & x \leq -t\sqrt{gh_0} \\ \frac{2}{3} \left( \sqrt{gh_0} + \frac{x}{t} \right) & , & -t\sqrt{gh_0} < x \leq t(u_2 - \sqrt{gh_2}) \\ u_2 & , & t(u_2 - \sqrt{gh_2}) < x \leq tS \\ 0 & , & tS \leq x \end{cases} \quad (27b)$$

The constant state values  $h_2$  and  $u_2$  and the shock speed  $S$  can be calculated for any initial conditions by solving

$$h_2 = \frac{h_0}{2} \left( \sqrt{1 + 8 \left( \frac{2h_2}{h_2 - h_0} \left( \frac{\sqrt{gh_1} - \sqrt{gh_2}}{\sqrt{gh_0}} \right) \right)^2} - 1 \right) \quad (28a)$$

$$u_2 = 2 \left( \sqrt{gh_1} - \sqrt{gh_2} \right), \quad (28b)$$

$$S = \frac{2h_2}{h_2 - h_1} \left( \sqrt{gh_0} - \sqrt{gh_2} \right). \quad (28c)$$

The initial conditions as well as the analytic solution are discontinuous. Due to the discontinuities the solutions to the initial conditions are not unique, as solving the momentum equation (1b) or the energy equation

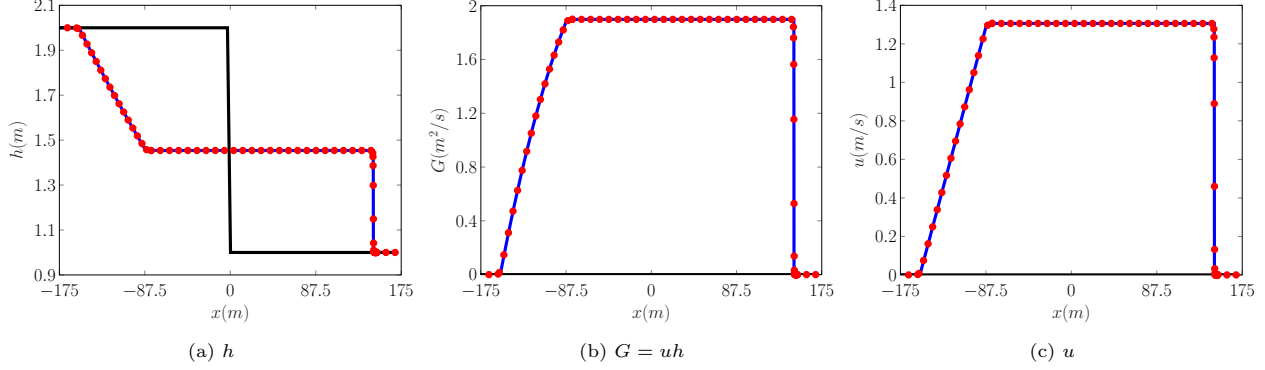


Figure 6: Comparison of initial (—), analytic solution (—), and numerical solution with  $\Delta x \approx 0.15m$  (•) to the dam-break problem for the gSGNE when  $\beta_1 = \beta_2 = 0$  at  $t = 35s$ .

(1c) results in solutions with similar structures but different shock speeds. The solution presented above is solution of the mass (1a) and momentum (1b) equations, as these equations are the basis of the numerical method.

A number of numerical experiments were run for the dam-break problem with  $h_0 = 2m$  and  $h_1 = 1m$ . The domain of the solution was  $[-250m, 250m]$  with a final time of  $t = 35s$ . The spatial resolution was varied like so  $\Delta x = 500/(100 \times 2^l)$  where  $l$  was increased from 0 to 12. To satisfy the CFL condition (22) the time step length  $\Delta t = \Delta x / (2\sqrt{gh_0})$  was used. The limiting parameter  $\theta = 1.0$  and the acceleration due to gravity  $g = 9.81m^2/s$  were used.

Example numerical solutions with the spatial resolution  $\Delta x = 500/(100 \times 2^5) \approx 0.15m$  and the analytic solutions for  $h$ ,  $G$  and  $u$  at the final time are plotted in Figure 6. These figures demonstrate that the method is robust in the presence of steep gradients and accurately reproduces the analytic solution.

The presence of discontinuities in the analytic solution makes accurately assessing convergence of the numerical solutions difficult. To circumvent these issues, the convergence measure has been restricted to comparing the numerical and analytic solutions for the constant region between the rarefaction fan and the shock. This modified convergence measure as  $\Delta x$  is varied is plotted in Figure 7a. This figure demonstrates that the scheme retains it's second-order accuracy away from discontinuities, as desired.

Since the analytic solution contains discontinuities all three conservation laws for  $h$ ,  $G$  and  $\mathcal{E}$  are not all satisfied simultaneously [22]. Since we solved equations for  $h$  and  $G$ , these quantities are conserved in the analytic solutions however,  $\mathcal{E}$  is no longer conserved and energy is lost as the shock propagates. Therefore, we introduce a new measure  $\mathcal{E}^*$  which measures the conservation error of the energy by comparing the total energy in the numerical solution with the total energy in the analytic solution at the final time. The conservation error for mass, momentum and energy as calculated normally and the new corrected energy are all compared in Figure 7b. This figure demonstrates that due to the use of the finite volume method even in the presence of discontinuities the conserved quantities  $h$  and  $G$  are conserved up to round-off error, leading to their conservation error increasing as  $\Delta x$  decreases. Energy is not conserved by the analytic solution, and this can be seen as the conservation error of  $\mathcal{E}$  does not improve as  $\Delta x$  decreases. However, when accounting for the lack of energy conservation by using  $\mathcal{E}^*$  we are able to recover first-order accuracy. Given that this solution contains a discontinuity these are good conservation results [30].

To further justify the ability of the method to resolve the discontinuous analytic solution, lower  $x_{\text{lower}}$  and upper  $x_{\text{upper}}$  bounds for the location of the shock in the numerical solution were found. These lower and upper bounds for the location are then used to bound the shock speed in the numerical solution. For  $x_{\text{lower}}$  this was accomplished by finding the first cell with  $\bar{h}_j \leq h_1 + \frac{9}{10}(h_2 - h_1)$  and for  $x_{\text{upper}}$  this was achieved by finding the first cell with  $\bar{h}_j \leq h_1 + \frac{1}{10}(h_2 - h_1)$ . Consequently, the lower bound for the shock speed  $S_-^* = x_{\text{lower}}/t$  and the upper bound for the shock speed  $S_+^* = x_{\text{upper}}/t$  were calculated and compared to the analytic value  $S$  given by (28c) in Figure 8. This figure demonstrates that as  $\Delta x$  decreases the numerical solutions better resolve the shock. Furthermore it demonstrates that  $x_{\text{lower}}$  and  $x_{\text{upper}}$  provide a bound for the true location of the shock.

These results demonstrate that the analytic solution of the SWWE has been accurately reproduced by the numerical method which solves the gSGNE with  $\beta_1 = \beta_2 = 0$ .

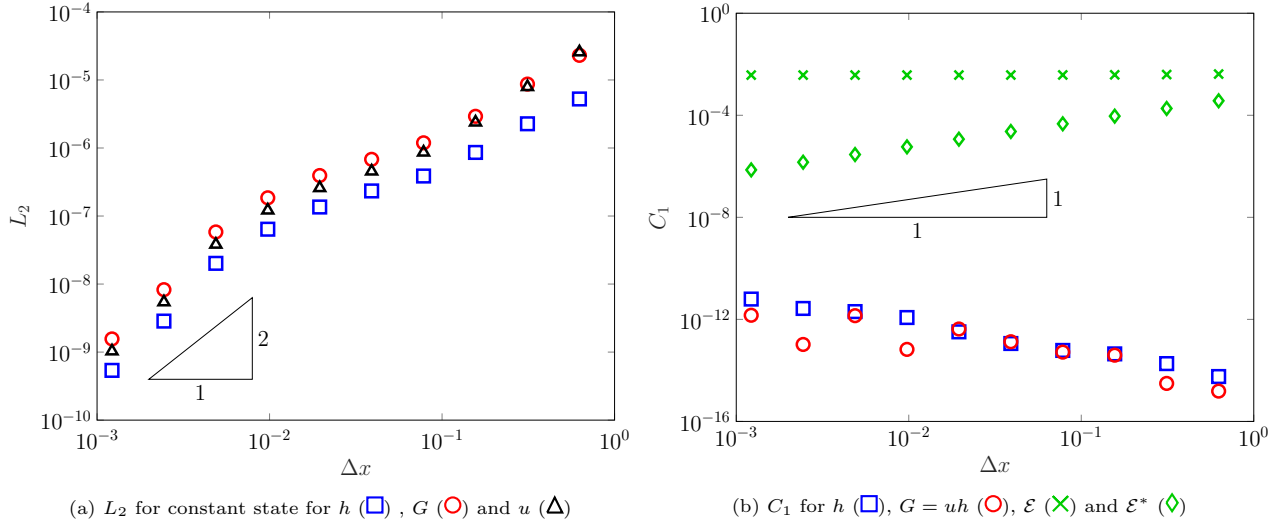


Figure 7: Convergence and conservation plots for the numerical solutions of the gSGNE when  $\beta_1 = \beta_2 = 0$  as  $\Delta x$  varies.

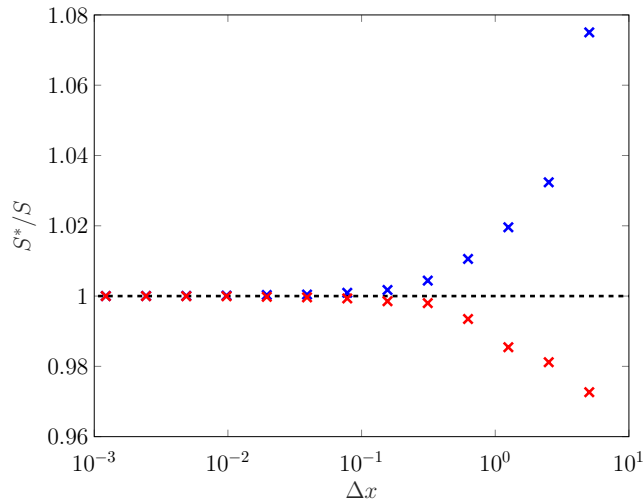


Figure 8: Plot of  $S_+^*/S$  (blue crosses),  $S_-^*/S$  (red crosses) and analytic value (dashed line) as  $\Delta x$  varies.



### 4.3. Forced Solutions

There are currently no known analytic solutions to the gSGNE for other  $\beta$  values. Hence, to demonstrate the validity and versatility of the method to solve the gSGNE for other  $\beta$  values, forced solutions are necessary. This is vital for the gSGNE in particular because for the  $\beta$  values tested above,  $\beta_2$  is always zero, and thus the known analytic solutions do not assess the numerical methods accuracy for the  $\beta_2$  term.

To generate a forced solution the forced gSGNE are considered

$$\frac{\partial h}{\partial t} + \frac{\partial(uh)}{\partial x} = \frac{\partial h^*}{\partial t} + \frac{\partial(u^*h^*)}{\partial x} \quad (29a)$$

$$\begin{aligned} \frac{\partial G}{\partial t} + \frac{\partial}{\partial x} \left( uG + \frac{gh^2}{2} - \beta_1 h^3 \frac{\partial u}{\partial x} \frac{\partial u}{\partial x} - \frac{1}{2} \beta_2 gh^2 \left[ h \frac{\partial^2 h}{\partial x^2} + \frac{1}{2} \frac{\partial h}{\partial x} \frac{\partial h}{\partial x} \right] \right) = \\ \frac{\partial G^*}{\partial t} + \frac{\partial}{\partial x} \left( u^* G^* + \frac{g(h^*)^2}{2} - \beta_1 (h^*)^3 \frac{\partial u^*}{\partial x} \frac{\partial u^*}{\partial x} - \frac{1}{2} \beta_2 g (h^*)^2 \left[ h^* \frac{\partial^2 h^*}{\partial x^2} + \frac{1}{2} \frac{\partial h^*}{\partial x} \frac{\partial h^*}{\partial x} \right] \right). \end{aligned} \quad (29b)$$

The forced gSGNE admit the solutions  $h^*$ ,  $u^*$  and  $G^*$  assuming  $G^*$  satisfies (9c). Since these equations are satisfied for any chosen functions for  $h^*$ ,  $u^*$  and  $G^*$  and any  $\beta$  values, forced solutions can be used to verify the method for a larger class of problems than permitted by currently known analytic solutions. Since the left hand-side of these modified equations are approximated by the numerical method, combining the numerical method with the analytic expressions for the right hand-side, produces a method that approximates the forced gSGNE (29) with the same convergence properties as the underlying numerical method for the gSGNE.

The following forced solution

$$h^*(x, t) = a_0 + a_1 \exp \left( \frac{(x - a_2 t)^2}{2a_3} \right) \quad (30a)$$

$$u^*(x, t) = a_4 \exp \left( \frac{(x - a_2 t)^2}{2a_3} \right) \quad (30b)$$

where  $G^*$  is given by (9c), were used. These forced solutions describe Gaussian bumps in  $h$  and  $u$  that travel at a constant speed  $a_2$ . This forced solution was chosen because it is smooth and the terms in (29) are not constant over the whole domain. Smoothness is necessary for the current description of the forced solutions, since it requires the derivatives to be defined in the classical strong sense. This ensures that the forced solutions include all the terms in the gSGNE when assessing the numerical method.

The particular parameter values  $a_0 = 1$ ,  $a_1 = 0.5$ ,  $a_2 = 5$ ,  $a_3 = 20$  and  $a_4 = 0.3$  were chosen in this investigation, while multiple  $\beta$  values were tested we will be focusing on  $\beta_1 = 2/15 + 2/3$  and  $\beta_2 = 2/15$  below. This choice of  $\beta$  values corresponds to the improved SGNE which have a  $\mathcal{O}(k^6)$  accurate dispersion relationship. There is an example numerical solution for these equations in Figure 1(c).

The numerical solutions were produced over the domain  $[-100m, 100m]$  with a final time of  $t = 10s$ . The spatial resolution was varied like so  $\Delta x = 200/(100 \times 2^l)$  with  $l$  varied from 0 to 11. To satisfy the CFL condition the time step size  $\Delta t = \Delta x / \left( 2 \left[ a_4 + a_2 + \sqrt{g(a_0 + a_1)} \right] \right)$  was chosen. The acceleration due to gravity  $g = 9.81m^2/s$  was used. For the forced solutions the limiting on the reconstruction on  $h$ ,  $u$  and  $G$  was removed. Because these forced solutions are smooth, such reconstruction is not necessary.

Figure 9 compares an example numerical solution at the final time for  $h$ ,  $G$  and  $u$  with  $\Delta x = 200/(100 \times 2^5) \approx 0.06m$  with the analytic solution. These example solutions demonstrate that the numerical method is able to reproduce the forced solution well, validating the numerical methods approximation to all terms in (9).

Figure 10 demonstrates the convergence of the numerical scheme as  $\Delta x$  decreases. All quantities of interest are converging at the expected second-order. Since the right hand-sides of (29) are evaluated analytically, the observed error is caused by the numerical method alone. Therefore, these results demonstrate that the scheme is second-order for all terms in the gSGNE.

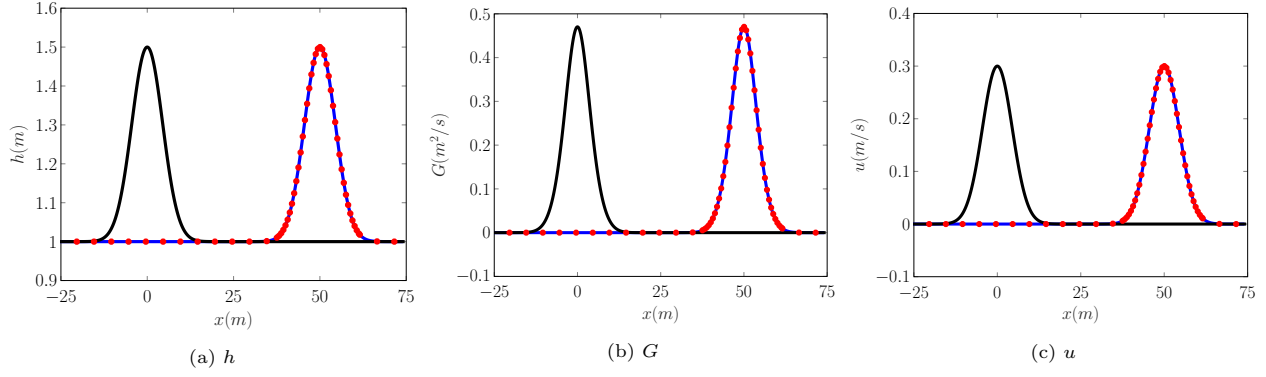


Figure 9: Plots of the initial conditions ( $\blacksquare$ ), analytic solution ( $\blacksquare$ ), and numerical solution with  $\Delta x \approx 0.06m$  ( $\bullet$ ) for the forced gSGNE with  $\beta_1 = 2/3 + 2/15$  and  $\beta_2 = 2/15$ .

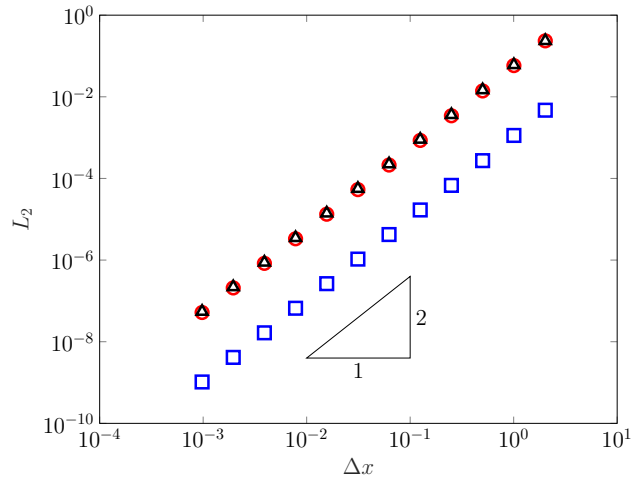


Figure 10: Convergence plot of  $h$  ( $\square$ ),  $G$  ( $\circ$ ),  $u$  ( $\Delta$ ) for the solutions of the forced gSGNE with  $\beta_1 = 2/3 + 2/15$  and  $\beta_2 = 2/15$  for various  $\Delta x$  values.

## 5. Experimental Comparison for Dispersive Shock Waves

The numerical solutions of particular members of the gSGNE family will now be compared to the experimental results of Hammack and Segur [31] which observed the evolution of an initial rectangular depression in the free surface. The experiments were conducted in a wave tank  $0.394m$  wide,  $31.6m$  long and  $0.61m$  high filled by water  $h_0 = 0.1m$  deep. The initial wave was generated by a  $0.61m$  long piston with its left edge flush with the left edge of the wave tank. The piston is originally in the up position with the water stationary, the piston is then dropped creating the rectangular depression in the surface, which generates a dispersive shock wave. The generated depression has its rarefaction fan component propagate up the wave tank, while the dispersive shock wave reflects from the left edge of the wave tank and then propagates up the wave tank. The evolution of the free surface is recorded over time by Wave Gauges (WG) located  $0m$  (WG1),  $5m$  (WG2),  $10m$  (WG3),  $15m$  (WG4) and  $20m$  (WG5) away from the right edge of the piston. Two heights of the generated rectangular wave were investigated  $h_0 - h_1 = 0.01m$  and  $h_0 - h_1 = 0.03m$  where  $h_1$  is the height of the water above the piston after it drops.

The rectangular wave experiments were modelled numerically by reflecting the problem around the left wall of the wave tank to reproduce the reflection off it. The initial conditions for this reflected problem are

$$h(x, 0) = \begin{cases} h_1 & |x| < 0.61 \\ h_0 & \text{otherwise} \end{cases}, \quad G(x, 0) = 0 \quad \text{and} \quad u(x, 0) = 0$$

which produces the depression above the piston reflected around the left edge of the wave tank. The numerical solutions were computed on a spatial domain of  $[-60m, 60m]$  from  $t = 0s$  to  $50s$  with acceleration due to gravity,  $g = 9.81m/s^2$ . The spatial resolution of  $\Delta x = 0.01m$  was used with a temporal resolution of  $\Delta t = 0.5\Delta x/\sqrt{g h_0}$  chosen to satisfy the CFL condition (22). The reconstruction limiting parameter  $\theta = 1.2$  was used in all numerical solutions. Three pairs of  $\beta$  values were used to demonstrate the effect of changing the dispersion relationship; the SWWE with  $\beta_1 = \beta_2 = 0$ , the classical SGNE with  $\beta_1 = 2/3$  and  $\beta_2 = 0$  as well as the improved dispersion SGNE with  $\beta_1 = 4/5$  and  $\beta_2 = 2/15$ .

The comparison of the numerical simulations and the experimental results for all wave gauges in the  $h_0 - h_1 = 0.01m$  and  $h_0 - h_1 = 0.03m$  experiments are plotted in Figures 11 and 12 respectively. The plots demonstrate that the numerical solutions arrive at the wave gauges earlier than the experiment due to physical effects not captured by the equations. The most significant is that the piston does not move vertically instantaneously and thus a perfectly rectangular wave profile is not produced, as demonstrated by WG1 for small times. Additionally, effects such as bed and side wall friction as well as fluid viscosity act to slow the advance of the wave train compared to the numerical solutions, as observed. Despite these factors the numerical solutions replicate the behaviour well.

The experimental results demonstrate the necessity of including dispersion when resolving the evolution of steep gradients in fluids. The non-dispersive SWWE solutions are inadequate at replicating the dispersive wave train generated in the experiment. However, the SWWE shock speed is capable of approximating the speed of the dispersive wave front for this experiment. Although, as the height of the rectangular wave increases the agreement deteriorates, and SWWE shock speed underestimates the speed of dispersive shock waves [9] as predicted by the modulation theory [4].

The numerical solutions to the classical SGNE with  $\beta_1 = 2/3$  and  $\beta_2 = 0$  compare well to other numerical solutions to this experimental set up reported by Zoppou et al. [20] and Pitt [21]. The numerical solutions to the SGNE reproduce the front of the dispersive wave train well, particularly for the  $h_1 - h_0 = 0.01m$  experiment, however this agreement worsens as time and the location of the wave gauge increases. The SGNE predict significantly more and higher oscillations in the tail of the dispersive wave train. This is due to their lack of diffusive physical effects, such as viscosity and wall friction which act to damp the dispersive wave train in the experiment [9]. Wave envelopes produced by the trends in oscillation height shown in the highlighted regions for all but the first wave gauge are longer and arrive later than the experimental results.

The most accurate results are obtained using the improved dispersion SGNE with  $\beta_1 = 4/5$  and  $\beta_2 = 2/15$ . The improved SGN, maintain the good agreement of the classical SGNE at the front of the dispersive wave train, and improve it everywhere else. In particular, the single oscillation observed at WG1 on the depression before the dispersive wave train arrives is in better agreement than the other equations. The improved SGNE also better replicate the low oscillation regions observed in the experimental results and thus better reproduce the associated wave envelopes and their speeds. The enhanced reproduction of observed wave envelopes is

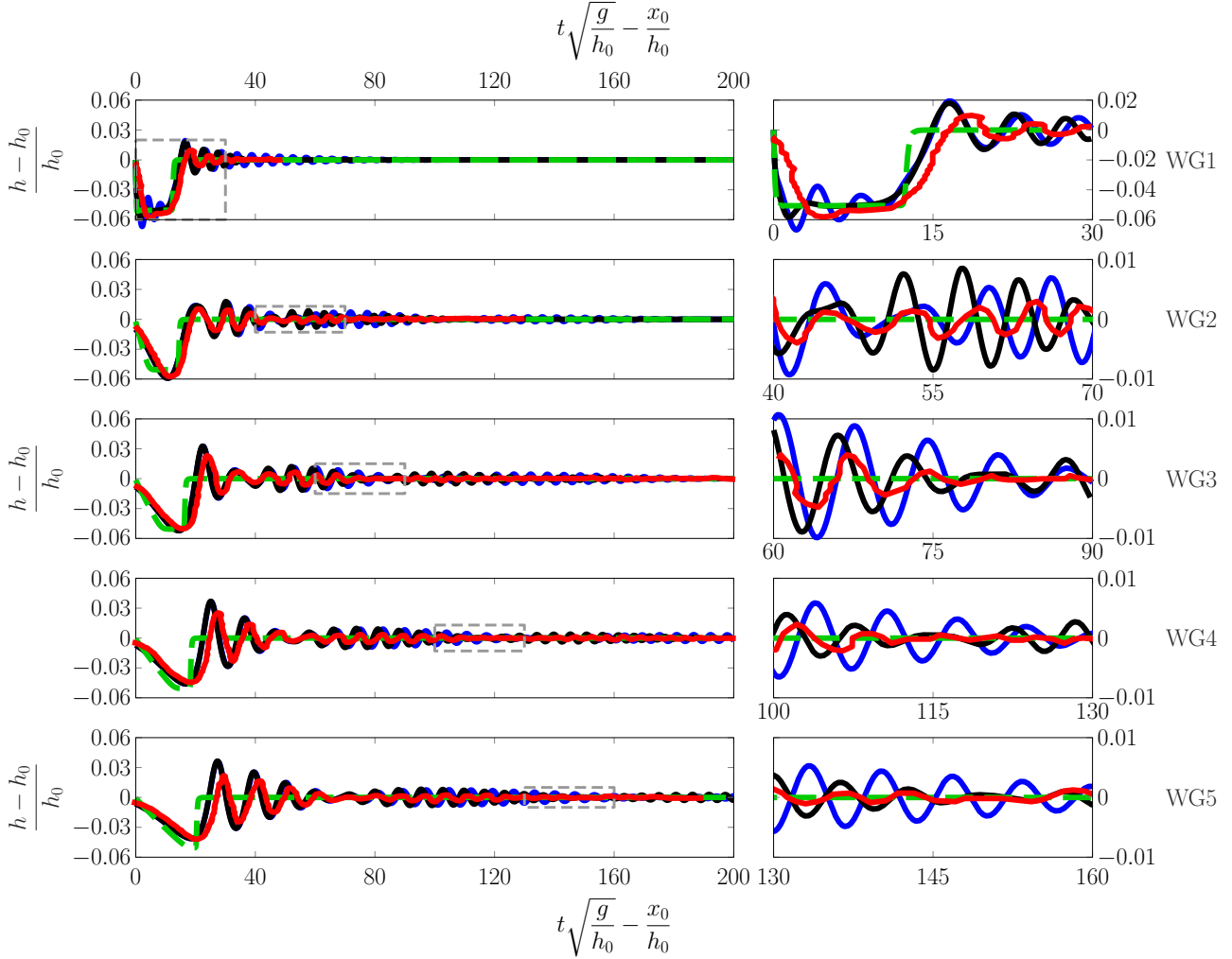


Figure 11: Rectangular negative wave experiments ( $h_0 - h_1 = 0.01m$ ) time series at the five Wave Gauges (WG) for simulation with the improved SGNE with  $\beta_1 = 2/3 + 2/15$  and  $\beta_2 = 2/15$  (—), the classical SGNE with  $\beta_1 = 2/3$  and  $\beta_2 = 0$  (—), the SWWE with  $\beta_1 = 0$  and  $\beta_2 = 0$  (—) compared to the experimental results (—). The left time series show the entire duration with highlighted region (—) shown on the right.

demonstrated in the highlighted regions of all but the first wave gauge for both experiments, showing the best replication of oscillation height trends. The improved SGNE produce the most accurate number and heights of oscillations, although the equations still overestimate them due to diffusive physical effects in the experiment not captured by the equations. The speed of these oscillations is also best matched by the solutions of the improved SGNE. These results for the improved dispersion SGNE agree with the findings of do Carmo et al. [32] for the evolution of an undular bore, which demonstrated the ability of the improved dispersion equations to best resolve the speeds and heights of the generated dispersive wave train. While the improved SGNE produce the best agreement, the experimental effects not included in the model are the dominant source of disagreement with numerical solutions.

The errors in conservation for all numerical simulations used to produce Figures 11 and 12 are displayed in Table 1. All numerical solutions conserve  $h$  and  $G$  to machine precision due to their use of a finite volume method. The energy  $\mathcal{E}$  is also well conserved by each numerical solution for both experiments, demonstrating that the numerical solutions are well resolved with the used spatial and temporal resolutions. However, larger rectangular waves do lead to worse conservation of energy.

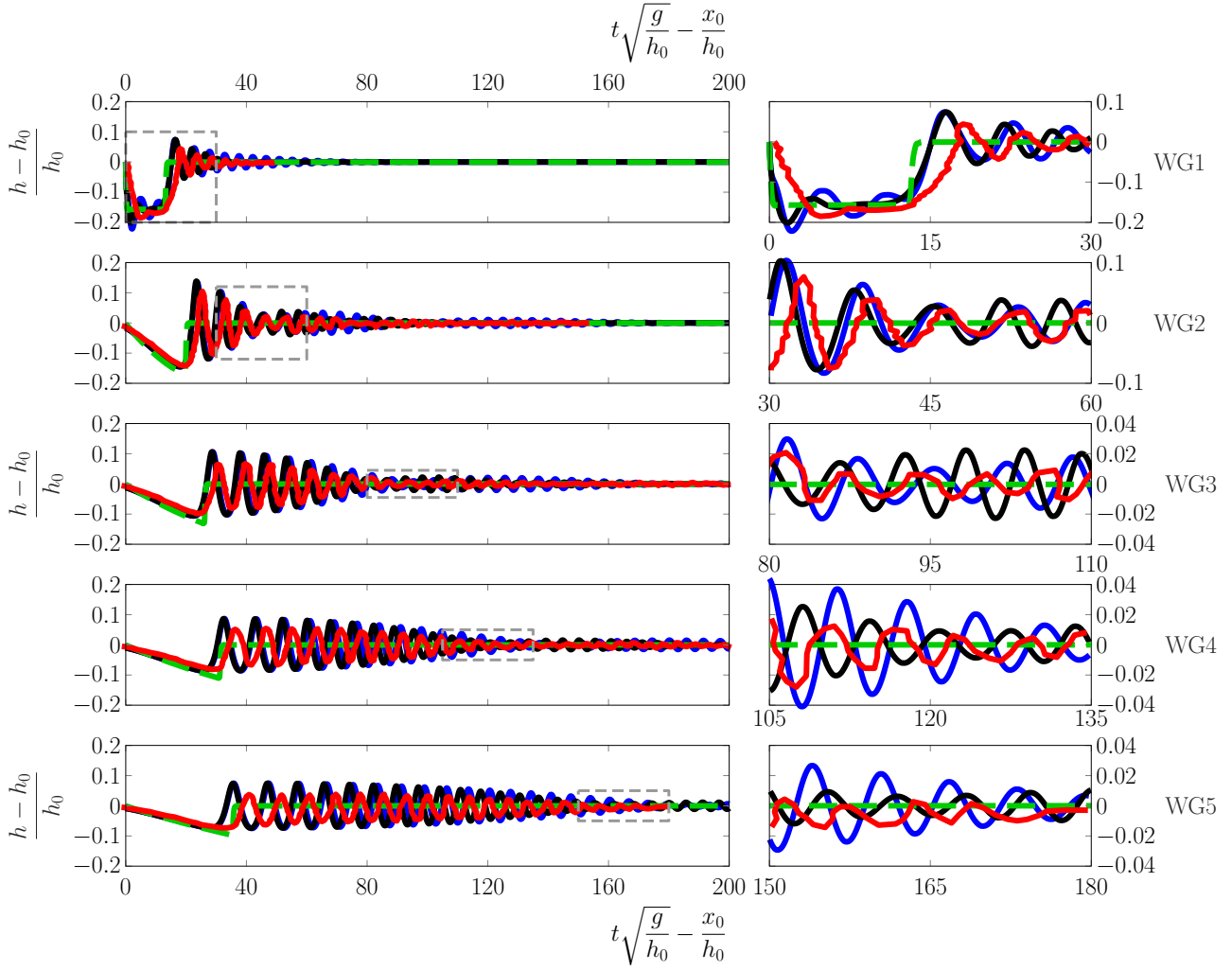


Figure 12: Rectangular negative wave experiments ( $h_0 - h_1 = 0.03m$ ) time series at the five Wave Gauges (WG) for simulation with the improved SGNE with  $\beta_1 = 4/5$  and  $\beta_2 = 2/15$  ( $\blackrightarrow$ ), the classical SGNE with  $\beta_1 = 2/3$  and  $\beta_2 = 0$  ( $\bluearrow$ ), the SWWE with  $\beta_1 = 0$  and  $\beta_2 = 0$  ( $\text{---}$ ) compared to the experimental results ( $\text{---}$ ). The left time series show the entire duration with highlighted region ( $\text{---}$   $\text{---}$ ) shown on the right.

$h_0 - h_1$	$\beta_1$	$\beta_2$	$C_1$ for $h$	$C_1$ for $G$	$C_1$ for $\mathcal{E}$
1cm	0	0	$6.238 \times 10^{-14}$	$9.648 \times 10^{-20}$	$4.939 \times 10^{-5}$
	2/3	0	$8.816 \times 10^{-14}$	$2.156 \times 10^{-17}$	$5.898 \times 10^{-6}$
	4/5	2/15	$8.949 \times 10^{-14}$	$1.056 \times 10^{-17}$	$1.579 \times 10^{-5}$
3cm	0	0	$5.286 \times 10^{-14}$	$3.221 \times 10^{-19}$	$6.577 \times 10^{-4}$
	2/3	0	$8.715 \times 10^{-14}$	$2.106 \times 10^{-17}$	$1.295 \times 10^{-4}$
	4/5	2/15	$8.403 \times 10^{-14}$	$1.528 \times 10^{-18}$	$2.364 \times 10^{-4}$

Table 1: Conservation of conserved quantities for numerical solutions to all negative rectangular wave experiments.

## 6. Conclusion

The gSGNE family of equations encompasses nonlinear wave equations from the non-dispersive SWWE to the improved dispersion SGNE by varying two free parameters  $\beta_1$  and  $\beta_2$ . This family of equations was classified using  $\beta_1$  and  $\beta_2$  according to the width and relative location of their dispersive wave trains using the dispersion relationship of the linearised equations. Example numerical solutions for select members of this family of equations were used to demonstrate that the full nonlinear gSGNE exhibit the same behaviour.

The numerical method used to generate these solutions was then described as a second-order implementation of a modified version of the numerical scheme for the SGNE outlined by Zoppou et al. [20]. The numerical method was validated against analytic solutions of the SGNE and SWWE and forced solutions. The analytic solutions demonstrate that the gSGNE solver accurately reproduces important members of the family of equations described by the gSGNE whilst conserving the quantities of interest. The forced solutions demonstrate that the method remains second-order for all values of the free parameters,  $\beta_1$  and  $\beta_2$ . The numerical solutions compared well to the experimental results for the evolution of a rectangular depression, with improved dispersion properties improving the reproduction of the experimental observations. The gSGNE method described above is the first validated numerical method for arbitrary members of the gSGNE family and its validation supports the provided classification of members of the gSGNE using their linear dispersive properties.

## References

- [1] B. Le Mehaute, An Introduction to Hydrodynamics and Water Waves, Springer Study Edition, 1st ed. 1976. ed., Springer Berlin Heidelberg, Berlin, Heidelberg, 1976.
- [2] R. Sorensen, Basic coastal engineering, 3rd ed., New York, NY Springer, 2006.
- [3] J. Kirby, F. Shi, B. Tehranirad, J. Harris, S. Grilli, Dispersive tsunami waves in the ocean: Model equations and sensitivity to dispersion and coriolis effects, *Ocean Modelling* 62 (2013) 39–55.
- [4] G. El, R. Grimshaw, N. Smyth, Unsteady undular bores in fully nonlinear shallow-water theory, *Physics of Fluids* 18 (2006) 027104.
- [5] D. Clamond, D. Dutykh, Non-dispersive conservative regularisation of nonlinear shallow water (and isentropic euler equations), *Communications in Nonlinear Science and Numerical Simulation* 55 (2018) 237–247.
- [6] F. Serre, Contribution à l'étude des écoulements permanents et variables dans les canaux, *La Houille Blanche* 6 (1953) 830–872.
- [7] G. B. Whitham, Non-linear dispersion of water waves, *Journal of Fluid Mechanics* 27 (1967) 399–412.
- [8] D. Clamond, D. Dutykh, D. Mitsotakis, Conservative modified Serre-Green-Naghdi equations with improved dispersion characteristics, *Communications in Nonlinear Science and Numerical Simulation* 45 (2017) 245–257.
- [9] J. Pitt, C. Zoppou, S. Roberts, Behaviour of the Serre equations in the presence of steep gradients revisited, *Wave Motion* 76 (2018) 61–77.
- [10] H. Dong, M. Li, A reconstructed central discontinuous Galerkin-finite element method for the fully nonlinear weakly dispersive Green-Naghdi model, *Applied Numerical Mathematics* 110 (2016) 110–127.
- [11] N. Panda, C. Dawson, Y. Zhang, A. B. Kennedy, J. J. Westerink, A. S. Donahue, Discontinuous Galerkin methods for solving Boussinesq-Green-Naghdi equations in resolving non-linear and dispersive surface water waves, *Journal of Computational Physics* 273 (2014) 572–588.
- [12] M. Li, L. Xu, Y. Cheng, A CDG-FE method for the two-dimensional Green-Naghdi model with the enhanced dispersive property, *Journal of Computational Physics* 399 (2019) 108953.
- [13] O. Le Métayer, S. Gavriluk, S. Hank, A numerical scheme for the Green-Naghdi model, *Journal of Computational Physics* 229 (2010) 2034–2045.

- [14] C. Zoppou, S. Roberts, J. Pitt, A solution of the conservation law form of the Serre equations, *The Australia and New Zealand Industrial and Applied Mathematics Journal* 57 (2016) 385–394.
- [15] D. Lannes, F. Marche, A new class of fully nonlinear and weakly dispersive Green-Naghdi models for efficient 2D simulations, *Journal of Computational Physics* 282 (2015) 238–268.
- [16] A. G. Filippini, M. Kazolea, M. Ricchiuto, A flexible genuinely nonlinear approach for nonlinear wave propagation, breaking and run-up, *Journal of Computational Physics* 310 (2016) 381–417.
- [17] J. do Carmo, J. Ferreira, L. Pinto, G. Romanazzi, An improved Serre model: Efficient simulation and comparative evaluation, *Applied Mathematical Modelling* 56 (2018) 404–423.
- [18] D. Dutykh, D. Clamond, P. Milewski, D. Mitsotakis, Finite volume and pseudo-spectral schemes for the fully nonlinear 1D Serre equations, *European Journal of Applied Mathematics* 24 (2013) 761–787.
- [19] C. Zoppou, Numerical Solution of the One-dimensional and Cylindrical Serre Equations for Rapidly Varying Free Surface Flows, Ph.D. thesis, Australian National University, Mathematical Sciences Institute, College of Physical and Mathematical Sciences, Australian National University, Canberra, ACT 2600, Australia, 2014.
- [20] C. Zoppou, J. Pitt, S. Roberts, Numerical solution of the fully non-linear weakly dispersive Serre equations for steep gradient flows, *Applied Mathematical Modelling* 48 (2017) 70–95.
- [21] J. Pitt, Simulation of Rapidly Varying and Dry Bed Flow using the Serre equations solved by a Finite Element Volume Method, Ph.D. thesis, Australian National University, Mathematical Sciences Institute, College of Physical and Mathematical Sciences, Australian National University, Canberra, ACT 2600, Australia, 2019.
- [22] Y. Pu, R. Pego, D. Dutykh, D. Clamond, Weakly singular shock profiles for a non-dispersive regularization of shallow-water equations, *Communications in Mathematical Sciences* 16 (2018) 1361–1378.
- [23] J. do Carmo, J. Ferreira, L. Pinto, On the accurate simulation of nearshore and dam break problems involving dispersive breaking waves, *Wave Motion* 85 (2019) 125 – 143.
- [24] M. Li, P. Guyenne, F. Li, L. Xu, High order well-balanced CDG-FE methods for shallow water waves by a Green-Naghdi model, *Journal of Computational Physics* 257 (2014) 169–192.
- [25] A. Kurganov, S. Noelle, G. Petrova, Semidiscrete central-upwind schemes for hyperbolic conservation laws and Hamilton-Jacobi equations, *Journal of Scientific Computing, Society for Industrial and Applied Mathematics* 23 (2002) 707–740.
- [26] S. Gottlieb, C. Shu, E. Tadmor, Strong stability-preserving high-order time discretization methods, *Review, Society for Industrial and Applied Mathematics* 43 (2001) 89–112.
- [27] S. Roberts, C. Zoppou, Explicit schemes for dam-break simulations, *Journal of Hydraulic Engineering* 129 (2003) 11–34.
- [28] S. Conte, C. De Boor, Elementary numerical analysis: An algorithmic approach, *International Series in Pure and Applied Mathematics*, 3rd ed., McGraw-Hill Inc., New York, 1980.
- [29] R. Courant, K. Friedrichs, H. Lewy, On the partial difference equations of mathematical physics, *IBM Journal of Research and Development* 11 (1967) 215–234.
- [30] C. Shu, Efficient algorithms for solving partial differential equations with discontinuous solutions, *Notices of the AMS* 59 (2012) 615–621.
- [31] J. Hammack, H. Segur, The Korteweg-de Vries equation and water waves. Part 3. Oscillatory waves, *Journal of Fluid Mechanics* 84 (1978) 337–358.
- [32] J. do Carmo, J. Ferreira, L. Pinto, G. Romanazzi, An improved Serre model: Efficient simulation and comparative evaluation, *Applied Mathematical Modelling* 56 (2018) 404–423.